Open Ceramics 23 (2025) 100804

Contents lists available at ScienceDirect

Open Ceramics

journal homepage: www.sciencedirect.com/journal/open-ceramics

The role of carbon presence on the strontium hexaferrite phase decomposition during pressureless spark plasma sintering (pSPS)

A. Učakar [a,b,c], A. Kocjan [a], B. Belec [d], J. Košir [e], T. Kallio [e], M. Kržmanc Maček [f], B. Arah [c], P. Jenuš Belec [a,*]

[a] Department for Nanostructured Materials, Jožef Stefan Institute, Ljubljana, Slovenia
[b] Jožef Stefan International Postgraduate School, Ljubljana, Slovenia
[c] Canter for Microscopy and Microanalysis, Jožef Stefan Institute, Ljubljana, Slovenia
[d] Materials Research Laboratory, University of Nova Gorica, Nova Gorica, Slovenia
[e] Department of Chemistry and Materials Science, Aalto University, Espoo, Finland
[f] Department for Advanced Materials, Jožef Stefan Institute, Ljubljana, Slovenia

ARTICLE INFO

Keywords:
Sr-hexaferrite
Sr-hexaferrite decomposition
Permanent magnets
pSPS
Magnetic properties
Numerical simulation

ABSTRACT

The phase composition and microstructure of Sr-hexaferrite (SFO) ceramics govern the hard magnetic properties. Here, pressureless spark plasma sintering (pSPS) technique was employed for the rapid consolidation (500 °C/min) of SFO in a radiating graphite crucible under vacuum and, thus, reductive conditions. A numerical model depicting the temperature profile within the heating crucible was constructed to understand the temperature evolution within the samples. The combination pSPS sintering environment (graphite heating crucible under vacuum) promoted phase decomposition to Sr-enriched and depleted phases of various morphological variations, leading to reduction of hard magnetic properties. Notably, certain newly formed phases exhibited lower melting points, inducing a shift in the sintering mechanism from solid-state sintering to a partial liquid-phase sintering mechanism.

1. Introduction

Development of permanent magnets that are indispensable in energy delivery and conversion systems [1] play an important role in the green transition. Particularly interesting are ceramic magnetic materials called M-hexaferrites (M = Ba, Sr, Pb), due to combination of their hard magnetic properties, good corrosion resistance and low production costs. The figure of merit for permanent magnets is maximum energy product (BH_{max}), which depends on remanence (M_r), coercivity (H_c) and the shape of the demagnetization curve. These values are of great importance for permanent magnets and are largely dependent on phase composition, microstructure and density. All these makes processing, phase stability and microstructural changes crucial in understanding, planning, and improving M-hexaferrites [2].

Conventional sintering of Strontium-hexaferrites (SFO) requires sintering in air at a temperature of 1200 °C with dwell time of several hours, to achieve ≥ 90 % of materials' theoretical density (TD) [3]. Magnetic properties achieved by conventional sintering are H_c 96 kA m^{-1}, M_r 55 Am^2 kg^{-1} and M_s 74.5 Am^2 kg^{-1} while microstructure indicates grain coarsening when compared to the starting powder. Consolidation by spark plasma sintering (SPS), which relies on applied pressure and current-induced rapid Joule heating, can substantially lower the sintering temperature and dwell time. Jenuš *et al.* reported successful SPS consolidation of SFO ceramics with refined grain structure, sintered at 900 °C for 5 min with an applied pressure of 92 MPa. Grain size in the sintered sample remained under 100 nm, total density of 4.84 g cm^{-3} was achieved (94 % of TD), while H_c was 167 kA m^{-1}, M_r was 65.8 Am^2 kg^{-1} and BH_{max} 21.9 kJ m^{-3} [4]. However, when it comes to the complex-shaped magnets SPS has geometrical limitations [23,24].

Provoking enhanced densification while still preserving near-net (cylindrical) shapes can be achieved by fast firing (FF), which was already established 1980's by Harmer et al. [25,26]. By using high heating rates, the ceramic specimen surpasses the low temperature surface-diffusion-controlled grain coarsening (the initial stage of sintering), immediately subjected to temperatures where the grain boundary (GB) and the lattice diffusion dominate (intermediate-to-final stage) [27]. The rapid sintering technique, which enables sintering of complex-shaped ceramics is pressureless spark plasma sintering (pSPS).

* Corresponding author.
E-mail addresses: aleksander.ucakar@ijs.si (A. Učakar), petra.jenus@ijs.si (P.J. Belec).

https://doi.org/10.1016/j.oceram.2025.100804
Received 28 February 2025; Received in revised form 13 May 2025; Accepted 27 May 2025
Available online 5 June 2025

pSPS process uses the Joule heating effect to elevate the temperature in the heating die, which is transferred to the sample via thermal radiation. One of the advantages of this fast-sintering technique is that it allows the retention of smaller grain sizes after consolidation when compared to conventional sintering [5].

To the best of our knowledge, pSPS process has not been used for consolidation of SFO yet, so our experimental planning leaned on the results of research conducted on Si_3N_4 [6] and ZrO_2 [7] and on scientific papers describing conventional [8] and SPS [9,10] sintering of SFO. In pSPS of ZrO_2 and Si_3N_4 the consolidation temperature was set approximately 100 °C higher than for the conventional sintering of those materials. While selecting pSPS sintering temperatures, one has to be careful not to exceed the phase decomposition temperature. N. Langhof described in detail the phase decomposition of SFO from M ($SrFe_{12}O_{19}$) to W ($SrMe_2Fe_{16}O_{27}$, Me stands for metallic ion) structure [19,28] when the temperature exceeds 1350 °C [11]. This phase decomposition is undesirable since in polycrystalline magnets leads to the degradation of hard magnetic properties. This study aimed to observe the phase evolution that occurs during pSPS sintering of the SFO. Chemical, morphological and magnetic changes in pSPS sintered samples were monitored using various analytical methods.

2. Materials and methods

2.1. Sample preparation

2.1.1. Starting powder

In this study, commercial strontium ferrite powder, SFO ($SrFe_{12}O_{19}$, 99 %), from Max Baermann GmbH (Germany) was used. Particle size was determined with the laser scattering particle size distribution analyser Horiba LA-920 (More data on the starting powder are given in Supporting information Figure S1). To remove large agglomerates, the SFO powder was sieved (sieve size 0.5 mm) before making the green pellets. Samples were consolidated by a uniaxial hydraulic press with a pressure of 100 MPa; the green pellets were cylindrical in shape, measuring 6 mm in diameter, 4 mm in height and 0.4 g in weight.

2.1.2. Consolidation

Shrinkage profile was determined by non-contact horizontal optical dilatometer Misura – Expert System Solutions. The dilatometric experiment was done in air atmosphere with a heating rate of 50 °C / min to the temperature of 1100 °C and retained at that temperature for 1 h, then the temperature was raised to 1200 °C and later to 1300 °C with the same heating rate and dwell time. Due to the restrictions of the dilatometer the experiments were not performed in vacuum. pSPS was done in SPS apparatus (Fuji Electronic Industrial Dr. SINTER SPS SYNTEX 3) with a modified cylindrically shaped graphite crucible. A schematic representation of the heating crucible is presented in Fig. 1a. At the bottom of the crucible is a 1 cm thick layer of graphite foam, positioning the sample in the geometric centre of the crucible. The sintering was done under vacuum in the following sequence: the crucible was heated to 600 °C in one minute and held at this temperature for one minute to achieve a homogeneous temperature distribution in the sample. Then, with a heating rate of 500 °C min^{-1}, the sample was heated to the sintering temperature of 1100 - 1300 °C (in the steps of 100 °C) and kept at that temperature for 5 min and then left to cool down rapidly (uncontrolled) after switching off heating (current). This is represented in Fig. 1b).

2.2. Characterization

Sintered samples' relative densities were determined by the geometrical method, taking into account that the theoretical density of SFO is 5.10 g cm^{-3} [12].

2.2.1. Phase composition and microstructure

The phase composition of starting powder and of sintered samples was analysed by X-ray diffraction (XRD, Empyrean X-ray diffractometer) on the cut and polished surface of the sample. The XRD measurement was performed in $2\theta = 10°$ to 60° with the step of 0.01, speed of 1° min^{-1}. The high-temperature X-ray diffraction measurements (HT-XRD (Malvern Panalytical, Cu-Kα1) combined with a high-temperature oven HTK 1200 N (Anton Paar GmbH)) were performed in a temperature range between 20 °C and 1200 °C, in increments of 100 °C, and a 10 °C min^{-1} heating rate between each step. Each step involved a 1 h dwell period, followed by a 1 h measurement from $2\theta = 10°$ to 70° The samples were analysed on an Al_2O_3 sample holder. Due to the restrictions of the equipment the experiments were performed in an ambient atmosphere. Two samples were prepared for HT-XRD analysis. The first sample served as a reference and consisted of pure *SFO* powder, while in the second sample, *SFO* was mixed with high surface graphite (TIMCAL TIMREX HSAG300) in a 90/10 (w/w %) ratio using a mortar and pestle (*SFO+C*). Data obtained by the XRD analyses were analysed with GSAS-II [13]. The thermogravimetric (TGA) and differential scanning calorimetry (DSC) analysis was performed with the Mettler Toledo TGA/DSC2 thermal analyser. The powders were placed in *an* Al_2O_3 crucible and heated up from 40 °C to 1200 °C, with a heating rate of 10 °C min^{-1}. The analysis was performed under a constant N_2 flow of 50 ml/min. The experiment for the analysis of the evolved gases during heating of the SFO+*C* sample was performed in another simultaneous thermal analyser (STA) Jupiter 449 (Netzsch GmbH) coupled with a 403C Aëoloss mass spectrophotometer (Netzsch GmbH) using TG/DTA sample holder and Al_2O_3 crucibles. The measurement was performed with a heating rate of 10 °C/min in an argon atmosphere (purity 99.99 %) with a gas flow of 50 ml/min. In order to ensure as much as possible the oxygen-free atmosphere system was evacuated with the rotary and turbomolecular pump before filling the instrument with argon (99.99 %) and starting the measurement. The microstructural analysis and chemical composition of starting powders and sintered samples were determined by scanning electron microscopy using the electron microscopes

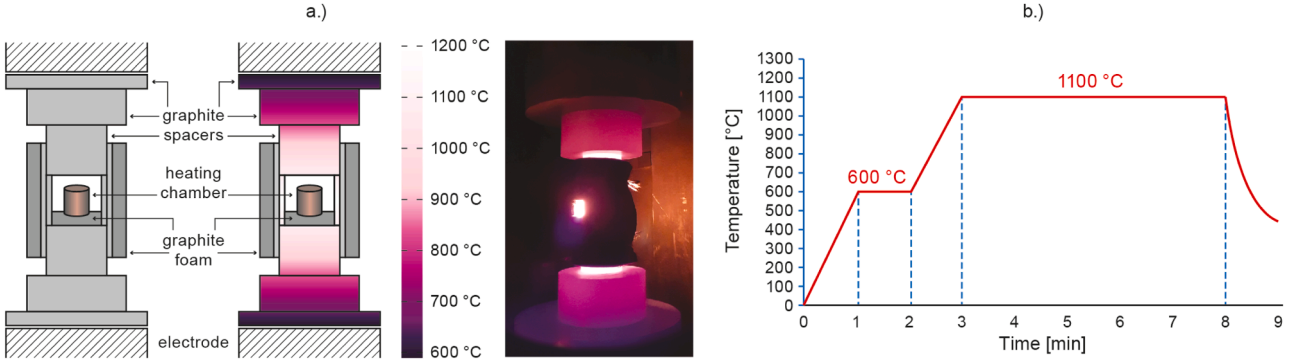

Fig. 1. Schematic representation of heating crucible with sample inside a.) and Thermal programme of sintering b.).

Jeol JSM-7600F, TermoFischer Quanta 650 ESEM equipped with an Energy dispersive X-ray spectroscopy detector (EDS - Oxford Instruments, AZtec Live, Ultim Max SDD 40 mm^2) and Termo Fischer Verios 4 G HP equipped with an Energy dispersive X-ray spectroscopy detector (EDS - Oxford Instruments, AZtec Live, Ultim Max SDD 65 mm^2).

2.2.2. Magnetic measurements

The magnetic properties of investigated materials were determined by vibrating sample magnetometer (VSM, Microsense EZ7).

2.3. Numerical modelling

Numerical simulations were done in the Abaqus/*CEA program*. For input data, the information obtained during pSPS experiments was used. An axisymmetric volumetric model in polar coordinates was described and presented in 2 dimensions and further optimized to represent half of the numerical model since we have axial symmetry. For heating the graphite crucible and spacers made from the same material we used the Joule heating effect equation (Eq. (1)).

$$W_+ = \frac{E^2 \pi r_0^2}{\sigma_0} \exp\left(\frac{Q}{R(T_0 + \Delta T)}\right) \quad (1)$$

Where W_+ stands for Joule heat, *E is applied electric field,* T_0 is furnace temperature, r_0 is radius of cylindrical specimen, σ_0 is resistivity pre-exponential, ΔT is the amount by the specimen temperature exceeds T_0, R is the gas constant and, Q is the activation energy for resistivity [14]. For a heat transfer mechanism between the heating body and the sample, we used the gap radiation principle in a vacuum (Eq (2)), which takes into account the mutual irradiation of internal surfaces in relation surface-to- surface radiation.

$$q_i^c = \frac{\sigma \epsilon_i}{A_i} \sum_j \epsilon_j \sum_k F_{ik} C_{kj}^{-1} \left((\theta_j - \theta^z)^4 - (\theta_i - \theta^z)^4 \right) \quad (2)$$

This formula is based on the grey body radiation theory [15]. Where q_i^c is thermal radiation, A_i is area of facet *i* seeing all cavity facets $j = 1, n$, ϵ_i . *i* represents location of interest (point of observation) while *j* represents all other surfaces, which are visible from point i (so radiation from surface i on all visible surfaces j). ϵ_j are emissivities of facets *i* and *j*, σ is Stefan-Boltzmann constant, F_{ij} is the geometrical view factor matrix,

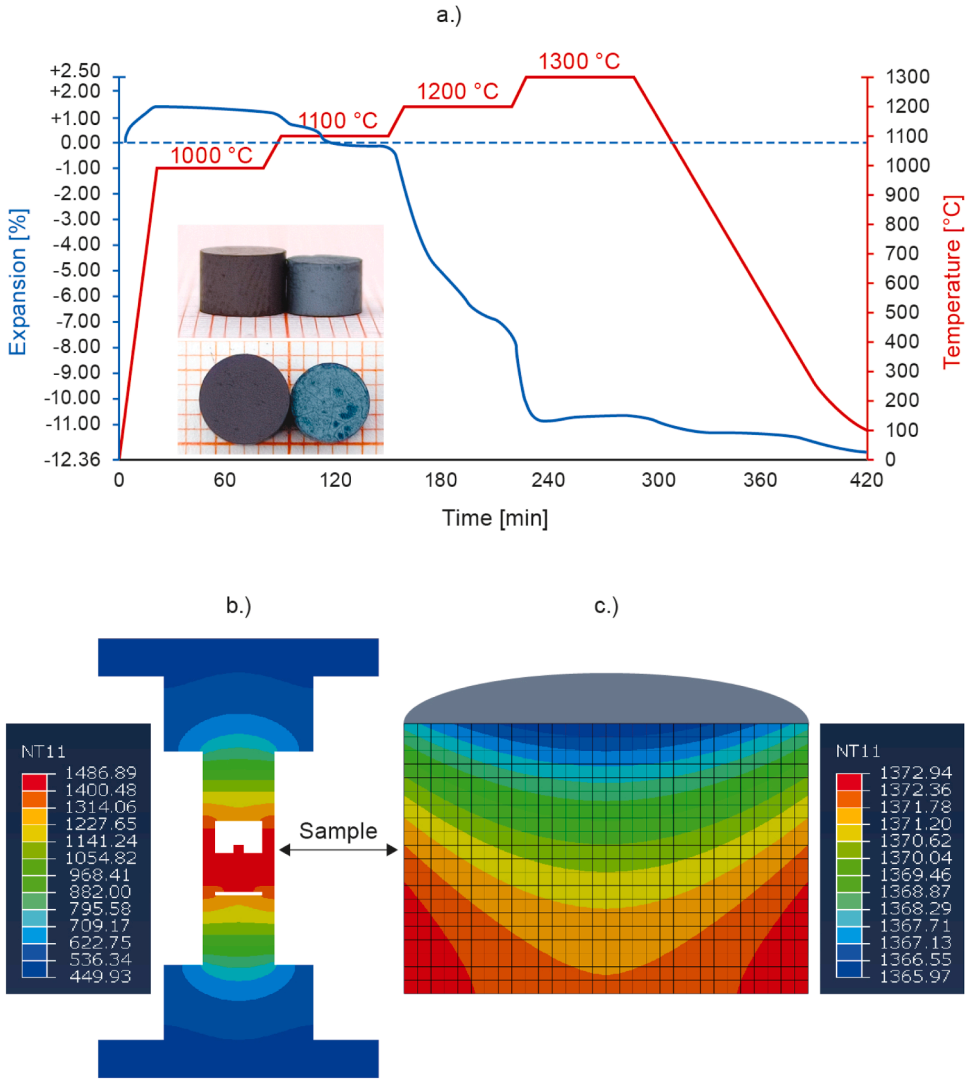

Fig. 2. a.) Dilatometric measurement of SFO during heating in air to different sintering temperatures with a heating rate of 50 °C per minute b.), numerical simulation of thermal profile based on radiative heating of the graphite heating die with a cylindrical sample positioned in the geometrical centre of the crucible by a graphite felt fundationand c.) cross-section view of thermal profile of cylindrical sample during pSPS at peak temperature. Data on numerical model are in Supporting info Table S1.

θ_i and θ_j are the temperatures of facets i and j, θ^z is the absolute zero on the temperature scale used and σ_{ij} is the Kronecker delta.

3. Results

3.1. Numerical modelling

The initial conditions for pSPS were determined from data obtained by the dilatometric analysis, which showed linear shrinkage between 1100 and 1200 °C and the steeper slope of the shrinkage curve at 1200 °C (Fig. 2a.)). Additionally, Fig. 2a shows the sample before and after sintering, as we can see it differs in both external dimensions and coloration. In the next step, the temperature profile in the graphite heating crucible was modelled by using numerical simulations (Figs. 2b and c.) showing temperature distribution of the crucible and sample temperature. It also indicates that the peak temperature of the sample inside the heating crucible is lower than the peak temperature of the heating crucible wall. For the simulation a set of data acquired during sintering of the sample to 1200 °C with a dwelling time of 5 min and a heating rate of 500 °C/min was used. However, the simulation did indicate that the heating in the chamber is not symmetrical and that the bottom part of the sample is being heated faster compared to other parts of the sample. Results of the numerical simulations suggest that the sample's bottom radial edge is roughly 7 °C hotter than its middle upper part. Additional laboratory experiments on all graphite "dummy models", tested the temperature difference between the graphite heating crucible surface and the sample positioned inside it. The measurement taken by thermocouple type-K, indicated only a small temperature difference (20.3 °C) between the two of them (T_{wall}=1083.7 °C vs. T_{sample}=1063.4 °C) in sintering test where the sample was heated to 1100 °C. It needs to be considered that the "dummy sample" was significantly larger due to placement issues connected with the thermocouple positioning, than the investigated samples. Because our samples are set on a layer of graphite felt a conduction between graphite heating crucible, graphite felt and SFO sample also play an important role in temperature profile evolution of the sample. It is implied by our simulations that a peak temperature of the sample inside (T_{sample}=1099.9 °C) the heating crucible is lower that the peak temperature of the heating crucible ($T_{crucible\ wall}$=1213.9 °C). This can be explained by position of the hottest part of the heating crucible wall being below the graphite felt layer. This suggests that the hottest point conducts the energy to the sample threw the graphite felt. This temperature difference is quite a sensible result considering the test measurements.

3.2. pSPS consolidated samples

3.2.1. Phase composition

The phase composition of pSPS sintered samples, determined by XRD, is presented in Fig. 3 and Table 1. The results show that the starting phase, $SrFe_{12}O_{19}$, decomposes into several phases during pSPS. Namely, in the samples sintered with pSPS at temperatures of 1100 °C and above, we can see the formation of strontium-rich ($Sr_3Fe_2O_7$) and strontium-depleted phases (FeO and Fe_3O_4). However, based only on the thermal stability of $SrFe_{12}O_{19}$ in air from pseudo-binary phase diagram, the decomposition should not occur up to ~ 1350 °C [11].

The geometrical densities of green and sintered samples are presented in Fig. 4a.). The increase in the sintering temperature increased the final densities, however, even with the highest sintering temperature of 1300 °C, the density was still lower than 90 % TD. Magnetic properties were determined on the as-sintered samples. The results are presented in Fig. 4b).

Table 1
XRD analysis of samples sintered with pSPS.

Sample	Phases			
1100 °C / 5 min	$SrFe_{12}O_{19}$			
1200 °C / 5 min	$SrFe_{12}O_{19}$			
1300 °C / 5 min		FeO	Fe_3O_4	$SrFe_2O_7$

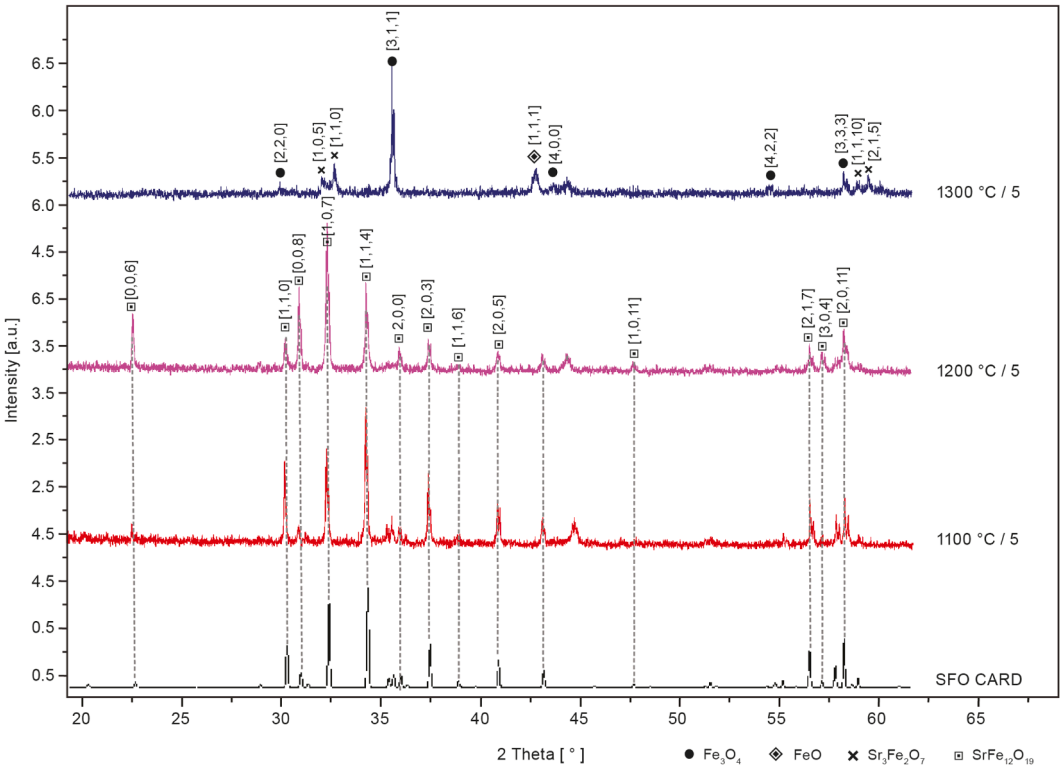

Fig. 3. XRD analysis of samples sintered with pSPS.

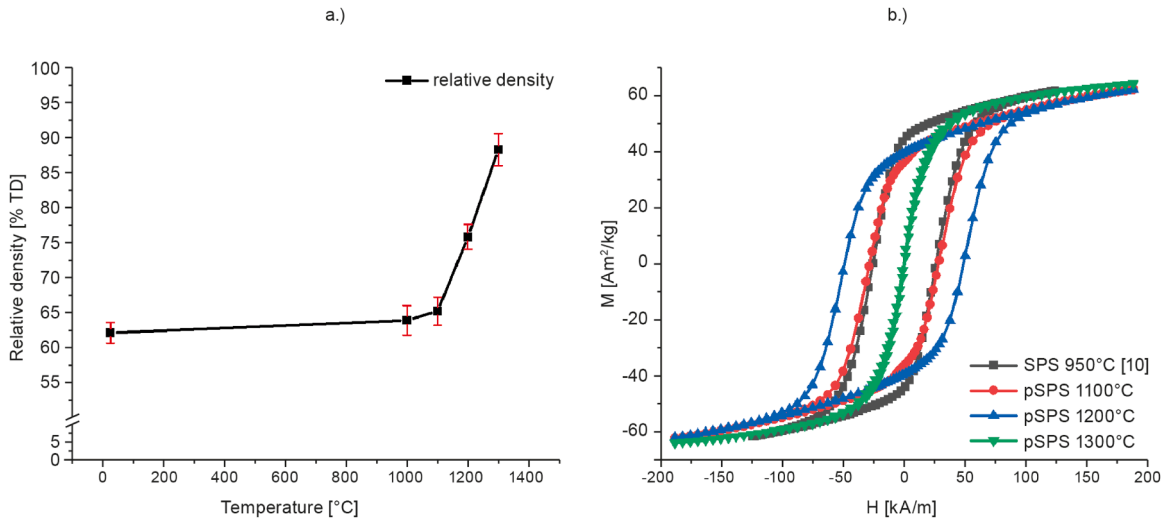

Fig. 4. a.) Geometrical densities of green and sintered samples and b.) magnetic properties of pSPS vs. SPS samples.

The formation of secondary phases, which do not have the same magnetic properties as SFO, was also observed via the magnetic measurements. A large decrease in coercivity in samples sintered at higher sintering temperatures (1300 °C) was observed indicating the formation of magnetically soft or paramagnetic materials i.e., various iron oxides (Fig. 4b)). For comparison, a magnetic hysteresis loop of the sample prepared from the same starting powder and sintered by SPS at 950 °C for 5 min with an applied pressure of 92 MPa (*Hc* 25.6 kA m^{-1}, *Mr* 44.1 $Am^2\,kg^{-1}$ and *Ms* 61.6 $Am^2\,kg^{-1}$) is presented in Fig. 4b) [10]. While the magnetic properties of the SPS sintered sample and the samples sintered by pSPS at 1100 °C, and at 1200 °C do not differ to a greater extent, there is a major difference in coercivity between the samples sintered by pSPS at 1100 °C for 5 min (H_C 50.2 kA m^{-1}, M_r 44.8 $Am^2\,kg^{-1}$ and M_S 65.9 $Am^2\,kg^{-1}$), and samples sintered by pSPS at 1300 °C for 5 min (H_C 0.4 kA m^{-1}, M_r 8.3 $Am^2\,kg^{-1}$ and M_S 64.0 $Am^2\,kg^{-1}$). Namely, a loss of coercivity and an increase in saturation magnetization has been observed for the sample sintered at 1300 °C. The latter indicates the decrease in the content of the hard magnetic phase (in our case SFO) and an increase in the soft magnetic phase (e.g., iron oxides).

3.2.2. *Microstructural analysis*

The microstructural analysis of sintered samples has revealed that the sintering temperature affected the porosity. At lower sintering temperature (1100 °C) an area of large porosity was observed in the middle of the samples (Fig. 5a). However, the sintering process has started, since the neck formation between grains is visible, but the formed necks were frequently cracked (marked with white arrows in Fig. 5a.). The cracking could be related either to the rapid cooling step or to the formation of various layers with different composition, density and thermal expansion coefficient which introduces tensile and compressive stresses to the material. After sintering, the samples exhibited a layered microstructure, as visible from the cross-section of the sample sintered at 1100 °C for 5 min (Fig. 5b)). The average thickness of the top layer (L1) measures about 39 μm in width, and has the highest observed density out of the three layers. The thickness of the sublayer (L2) is on average 92 μm. The two layers that form the outer rim have in common the formation of a lighter and a darker phase. SEM-EDS point analysis shown in Fig. 5 and Table 2 indicates the differences in the concentration of Sr and Fe in the two layers compared to the bulk of the pellet (layer 3, L3). The surface layer is Sr-enriched and slightly Fe-depleted, while the intermediate layer is Sr-depleted and slightly Fe-enriched. The concentration of O remains comparable in all three layers. This is all pointing to SFO decomposition. When calculated, the atomic ratios correspond to the following known Sr-Fe oxides from SEM-EDS: in L3 the starting material $SrFe_{12}O_{19}$ is present, area L2 contains $Sr_3Fe_{26}O_{41}$ and the upper layer (L1) is a mixture of $Sr_3Fe_{26}O_{41}$ and Fe_2O_3. A similar reduction of M-hexaferrite during SPS was proposed by Ovtar *et al.* for Ba-hexaferrite [16]. In order to obtain denser samples, the sintering temperature was raised to 1300 °C. However, the higher sintering temperature introduced more energy into the system and thus accelerated the decomposition of $SrFe_{12}O_{19}$.The microstructure of the sample sintered at 1300 °C for 5 min with a heating rate of 500 °C min^{-1} is displayed in Fig. 5.

The large area SEM image displays the cross-section of the sintered sample (Fig. 5c.)), where we can see the phase decomposition of the starting material into the secondary phases, the inhomogeneity of the microstructure, the remnant porosity and radiational cracking. Formation of 4 distinct phases can be observed in (Fig. 5d), where blue represents Iron oxides, green is $SrFe_{12}O_{19}$, red is $Sr_3Fe_2O_{6.73}$ and yellow is $SrFeO_3$. In the bulk of the sample (Fig. 5e, c and d), we observed the coarse growth of crystal grains and the formation of at least two phases. Grain coarsening was observed in the interior of the sample, while grains closer to the surface remained smaller, although the whole sample decomposed from SFO. A formation of two brighter phases (red and yellow in Fig. 6b)) was observed between larger darker grains. From the microstructure, it can be deduced that brighter phases containing more Sr have lower melting points and form a liquid phase, which embeds larger grains. This also causes the transition of the consolidation mechanism from solid state sintering to partial liquid phase sintering. Fig. 5f.) shows the distribution of strontium in the examined sample. Sr-rich and Sr-depleted areas can be observed. By comparing secondary electron images with EDS map analyses (Figs. 5f.)) it was deducted that the large darker grains are depleted of Sr, while the brighter coloured material between the grains is Sr-rich. This, however, has not been observed for the sample sintered at 1100 °C for 5 min.

The samples sintered at 1300 °C for 5 min were additionally re-oxidized at 1000 °C ($SrFe_{12}O_{19}$ annealing temperature for minimized grain growth [31]) in air atmosphere either for 1 h or 4 h. Microstructure in the re-oxidized sample has experienced changes compared to the test sample. The $SrFe_{12}O_{19}$ decomposition is partly reverted, the microstructure in bulk becomes more homogeneous, while the surface layer becomes thinner. A coalescence of pores in surface layer is observed in the process of re-oxidation. There is a diminishing of the number of pores on account of pore growth after 1 h of re-oxidation and after 4 h of re-oxidation the pores in surface layer disappear and the material densifies (Supporting Information Figure S3).

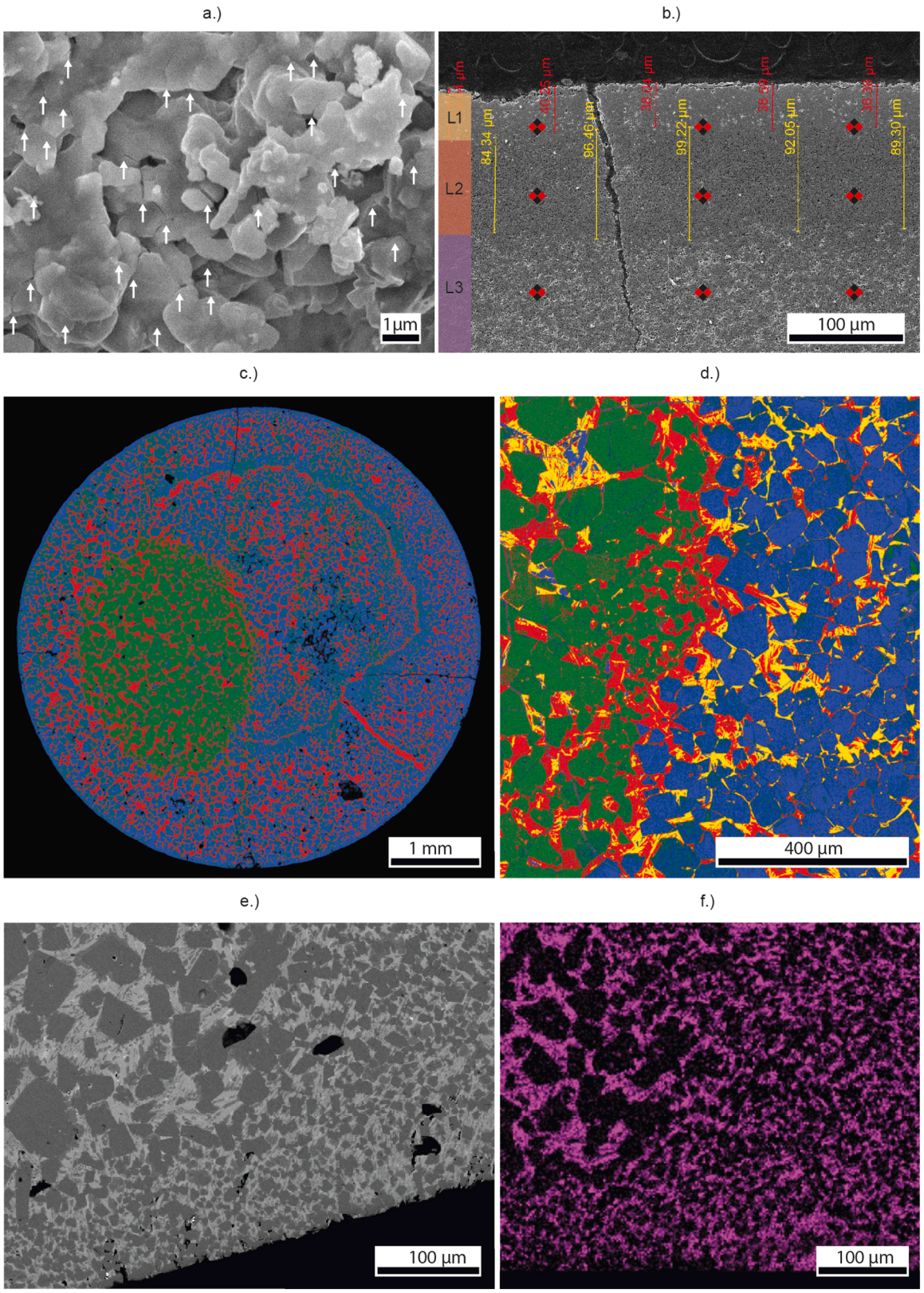

Fig. 5. a.) Middle part of SFO sample sintered by pSPS at 1100 °C with dwelling time of 5 min and heating rate of 500 °C min^{-1}. Arrows indicate the cracking of material, b.) SFO sample edge after pSPS sintering at 1100 °C $5min^{-1}$ – the formation of L1/2/3 layers. The dots represent points of EDS analyses, c.) SFO pellet after pSPS sintering at 1300 °C for 5 min^{-1} - Large area SEM coloured image and d.) SFO pellet after pSPS sintering at 1300 °C for 5 min^{-1} - SEM coloured image (blue represents Iron oxide, green is $SrFe_{12}O_{19}$, red is $Sr_3Fe_2O_{6.73}$ and yellow is $SrFeO_3$), e.) backscatter electrons image of samples' edge of SFO pellet after pSPS sintering at 1300 °C for 5 min^{-1}, and f.) EDS Sr-phase map of the area of SFO pellet after pSPS sintering at 1300 °C for 5 min^{-1}.

Table 2
SEM-EDS point analysis.

	Sr [at %]	Fe [at %]	O [at %]
L1	5.9 ± 0.3	35.3 ± 0.3	58.8 ± 0.3
L2	1.8 ± 0.3	38.5 ± 0.3	59.6 ± 0.3
L3	3.3 ± 0.3	37.3 ± 0.3	59.3 ± 0.3

3.2.3. *Diffusion couple and thermal analysis of $SrFe_{12}O_{19}$-C in air*

The Sr-ferrite decomposition should not occur up to 1350 °C [11], but phase composition and microstructural analysis have revealed that during pSPS of SFO in a graphite die, in vacuum the decomposition of SFO does occur. Therefore, the simulated environment for SFO surrounded by graphite was designed. Two samples were prepared, one containing SFO and one containing SFO powder mixed with 10 wt % of high surface graphite (SFO+*C*). The results of HT-XRD measured in air are presented in Fig. 6 and Table 3. The reference sample measurements and description are presented in Supporting information in Figure S2.

The reference (SFO) sample which was composed of only SFO powder did not show any difference in phase composition between RT and 1000 °C (Supporting information Figure S2). The analysis of the SFO+*C* sample (Fig. 6), that has been performed in the temperature range between RT and 1000 °C, has shown that graphite reacts with SFO and causes its decomposition into other iron-strontium oxides. Similarly, the decomposition of SFO was observed in pSPS sintered samples. However, not all the phases that formed in the SFO—C diffusion couple, determined by HT-XRD, are present in the pSPS samples due to the variation of the sintering temperature, atmosphere, and also carbon concentration.

The concentration of carbon in the simulated environment was deliberately excessive, in order to confirm the hypothesis that graphite from the graphite foam below the sample and the crucible walls plays an important role in the samples' final composition. The HT-XRD results suggest that the decomposition of SFO happens in three stages. The first stage can be considered as a stable zone between room temperature and 600 °C. This is followed by a transition zone between 600 °C and 900 °C in which the $SrFe_{12}O_{19}$ decomposes to several metastable phases due to the reductive surroundings. The final stage is a transition to γ-Fe, Fe_3O_4 and $SrFeO_{x-3}$.

First, $SrFe_{12}O_{19}$ partially decomposes to magnetite at 500 °C. At 600

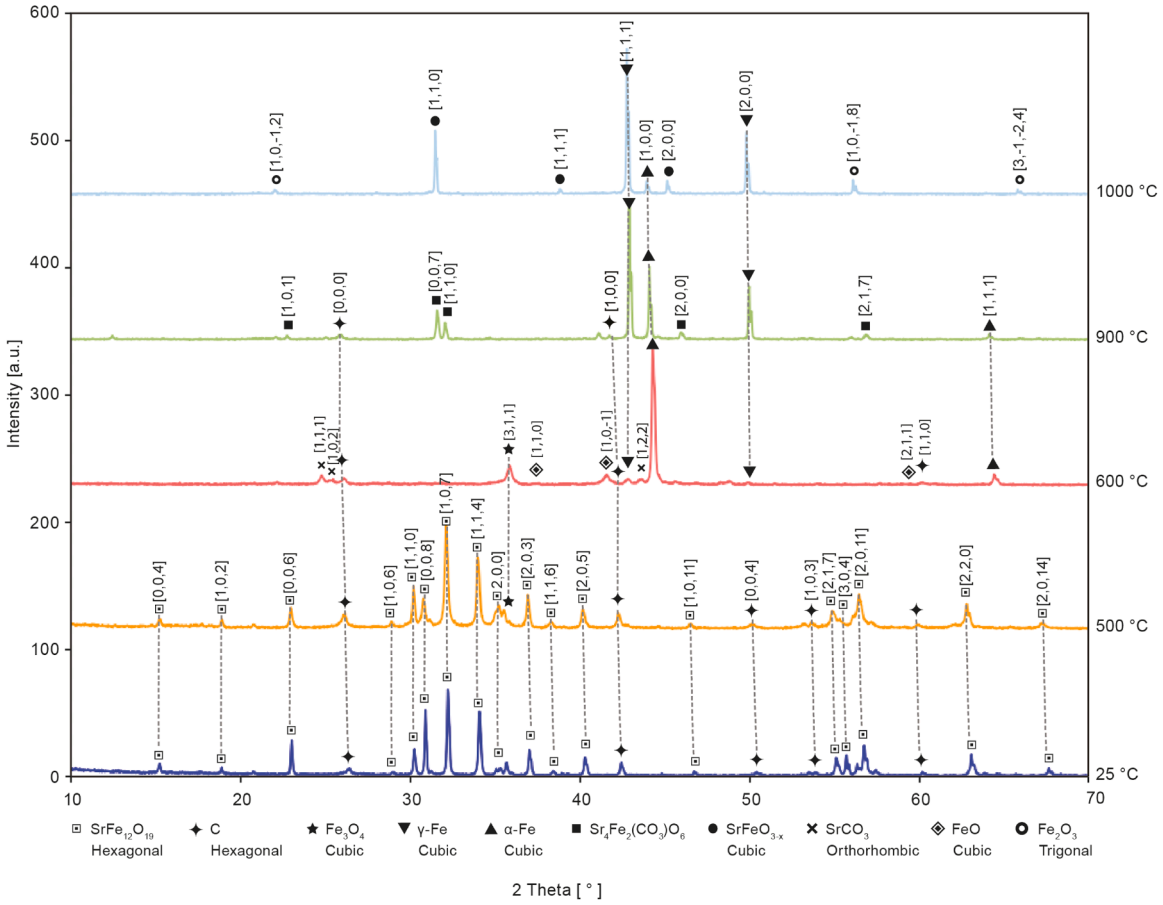

Fig. 6. Powder x-ray diffraction patterns detailing the phase evolution of the diffusion couple $SrFe_{12}O_{19}$ (SFO) with 10 wt % of C with varying temperature. Stable area up to 500 °C, metastable transformation between 600 °C and 900 °C to six different phases. When reaching 1000 °C four phases remain.

Table 3
Phase evolution of $SrFe_{12}O_{19}$ (SFO) with 10 wt % of C.

T	Phases									
25 °C	SFO	C								
500 °C	SFO	C								
600 °C		C		Fe_3O_4	FeO	α-Fe	γ-Fe	$SrCO_3$		
900 °C		C				α-Fe	γ-Fe	$SrCO_3$	$Sr_4Fe_2(CO_3)O_4$	
1000 °C			Fe_2O_3			α-Fe	γ-Fe			$SrFeO_{3-d}$

°C we already notice a reduction of Fe_3O_4 to FeO, α-Fe and γ-Fe. Additionally, the presence of $SrCO_3$ was observed, while no trace of $SrFe_{12}O_{19}$ is left at that temperature. At 700 °C α-Fe, γ-Fe, $SrCO_3$, and FeO are present. FeO disappears at 800 °C, and the ratio between α-Fe and γ-Fe starts to favour the formation of γ-Fe. At 900 °C a metastable phase $Sr_4Fe_2(CO_3)O_6$ is observed. When reaching 1000 °C the HT-XRD shows the presence of only α-Fe and γ-Fe in addition to $SrFeO_{x-3}$, while carbon is no longer detected. The results of HT-XRD analysis of SFO—C system were also in accordance with the phase diagrams: Sr-Fe-O, Fe-Sr and Fe-C [17,18].

The thermogravimetric analysis (TGA) and differential scanning calorimetry (DSC) of SFO and SFO+*C* are presented in Fig. 7.

Fig. 7a shows the TG and DSC curves of the pure SFO sample. The overall mass change, represented by the blue solid line, is minimal—only ~0.2 %. Visible mass variations over the heating range correspond to the measuring error of the method. However, the DSC curve (dotted black line) indicates that the mass variations, especially above 600 °C results from the endothermic reactions.

Fig. 7b presents the TG and DSC curves for the SFO + 10 % C sample. In contrast to pure SFO, this sample undergoes a considerably greater total mass loss of ~25 %. The TG curve remains relatively stable up to ~760 °C, except for a minor drop near 110 °C, again due to the desorption of surface-bound water (<0.5 %). A sharp mass reduction is observed between 760 °C and 920 °C, corresponding to a broad endothermic signal in the DSC curve, indicative of an energy-consuming (endothermic) reaction. This temperature range also aligns with the phase transformation observed in the XRD analysis. A more distinct endothermic peak appears between 1000 °C and 1050 °C, which is likely related to the formation of an additional phase. Above 1100 °C, both the TG and DSC signals level off, suggesting the end of significant thermal activity. Overall, the thermal behaviour of the SFO + 10 % C system differs markedly from that of pure SFO, highlighting the substantial impact of carbon addition on the decomposition of SFO and phase evolution processes.

Additionally, the MS analysis of SFO-10C measured in argon confirmed the formation of CO_2 ($m/z = 44$) at temperatures between 800 and 1000 °C (see Supporting information Figure S3). These further indicates that carbon reacts with oxygen in SFO, causing SFO decomposition. The decomposition is then further promoted by the formation of reductive species (CO) which additionally accelerate it. The peak intensity of CO_2 $m/z = 44$ with respect to that of $m/z = 28$ is comparable to that in the theoretical mass spectrum of CO_2. This indicates that formed CO, which exhibits the most intense fragment CO_2 $m/z = 28$, immediately react with Fe_3O_4 and FeO, producing CO_2 together with FeO (Eq. (6)) and Fe (Eq. (7)), respectively. This is also in accordance with the observed phase compositions (Table 3). The level of O_2 in the system was very low (ion current 10^{-11} A) and did not change significantly in the temperature range of CO_2 evolution, which is an additional sign that carbon reacts with the oxygen from the SFO lattice and not with O_2 present in the instrument (argon purity 99.999 %, removal of the ambient atmosphere with turbo molecular pump) (Figure S3).

4. Discussion

As a comparison, conventional sintering of Sr-hexaferrites (SFO) requires sintering in air at a temperature of 1200 °C with a dwell time of 4 h to achieve ≥ 90 % of the material's theoretical density (TD) [3]. pSPS is a fast densification technique of ceramics that allows for pressure-less sintering of complex shaped parts. In this research we have for the first-time consolidated strontium hexaferrite by pressureless spark plasma sintering. Samples sintered at 1300 °C for 5 min achieved high density (more than 85 % TD). However, the material underwent phase decomposition. Based on the obtained results, there is evidence that a reduction of $SrFe_{12}O_{19}$ caused by slightly reductive graphite and vacuum environment has occurred and segregated strontium hexaferrite to several different oxides. From the microstructure, it can be deducted that Sr-rich phases have lower melting points and surround larger grains. This also indicates a transition of the consolidation mechanism from solid state sintering to partial liquid phase sintering. Jin *et al.* [29] investigated microwave sintering of SFO in, so called, micro vacuum (p = 0.025 ~ 0.03 MPa) and in air flow. Regardless of the investigated atmosphere, the XRD analysis showed presence of SFO only. On the other hand, Bohlender et al. [30] studied the sintering of SFO in reducing atmosphere (Ar-5 % H_2) and they have observed partial decomposition of SFO at already 400 °C. Ba-hexaferrite has a very similar structure and properties to SFO, and Ovtar *et al.* [16], explained its decomposition during SPS. Following their interpretation, the following chemical reduction equations (Eqs. (3)-(5)) of this system are proposed [16].

$$9SrFe_{12}O_{19} \rightarrow 3Sr_3Fe_{26}O_{41} + 10Fe_3O_4 + 4O_2 \quad (3)$$

$$6Sr_3Fe_{26}O_{41} \rightarrow 18SrFe_2O_4 + 40Fe_3O_4 + 7O_2 \quad (4)$$

$$3SrFe_2O_4 + 3CO \rightarrow 3SrCO_3 + 6Fe + 3O_2 \quad (5)$$

Both $Sr_3Fe_{26}O_{41}$ and Fe_3O_4 phases are in accordance with the data obtained by SEM-EDS analysis, Fe has been proven to be in the SFO+*C* system at temperatures above 900 °C by XRD and HT-XRD. Furthermore, TG analysis has shown a roughly 25 % weight loss which indicates that a significant part of the reactant is lost and the formation of gaseous by-products is probable.

As such it is proposed that O_2 the product of Eqs. (3), 4 and 5 reacts

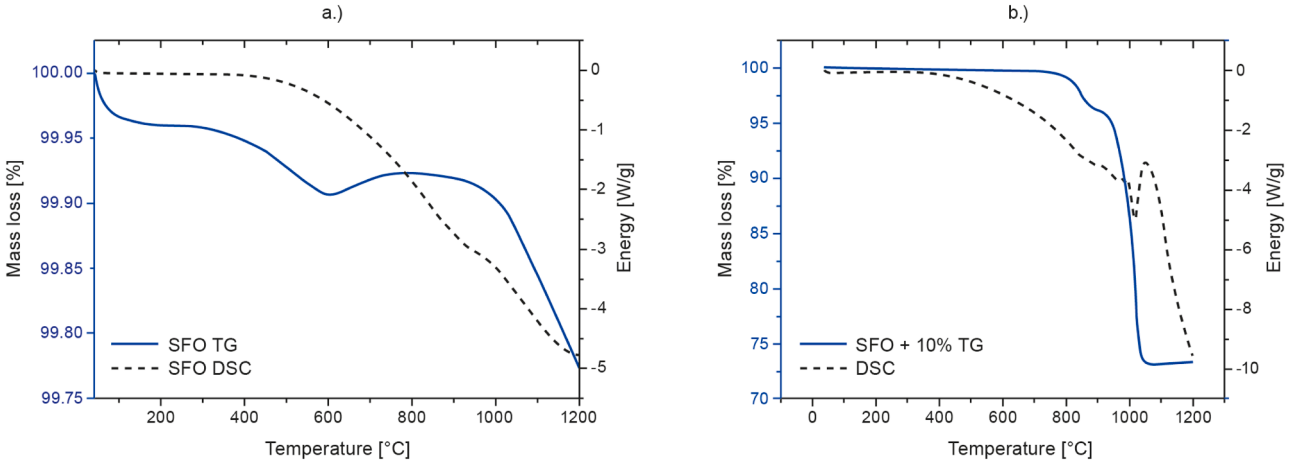

Fig. 7. TGA and DSC analysis of a.) SFO and b.) SFO+*C* sample.

with the graphite in the sample and forms CO. The formation of CO then leads to the indirect reduction of iron oxides. For this the following reactions are proposed (*Eqs. 6 and 7*):

$$Fe_3O_4 + CO \rightarrow FeO + CO_2 \quad (6)$$

$$FeO + CO \rightarrow Fe + CO_2 \quad (7)$$

Furthermore, due to the dynamic vacuum in the heating chamber during the sintering process, the low pressure surrounding the sample and considering the phase stability of $SrCO_3$ in vacuum, given by Bagherisereshki *et.al.* [20] the following equation is proposed (*Eq. (8)*)

$$SrCO_3 \rightarrow SrO + CO_2 \quad (8)$$

This explains the presence of simple iron- (Fe_3O_4, FeO, Fe) and strontium- ($SrCO_3$, SrO) based compounds in the HT-XRD sample at temperatures higher than 900 °C. In addition to that, for higher sintering temperatures (>1000 °C), A. Fossdal *et.al.* [21] proposed (*Eqs. (9)and (10)*) that Sr_2FeO_{4-d} and $Sr_4Fe_3O_{10-d}$ decompose according to:

$$2Sr_2FeO_{4-d} \rightarrow Sr_3Fe_2O_{7-d} + SrO + O_2 \quad (9)$$

$$Sr_4Fe_3O_{10-d} \rightarrow Sr_3Fe_2O_{7-d} + SrFeO_{3-d} + O_2 \quad (10)$$

The proposed chemical reactions between phases are in accordance with the pseudo-binary phase diagram SrO-Fe_2O_3 [11] if the reduction of the material is considered due to the high carbon content in the SFO+10 %C sample. VSM measurements of sintered samples also confirmed the decomposition of the $SrFe_{12}O_{19}$ to several oxides with different (soft) magnetic properties.

5. Conclusions

SFO was rapidly consolidated (500 °C/min) with a pressureless spark plasma sintering (pSPS) apparatus, using radiating graphite crucible under vacuum and, thus, reductive conditions. Since this was the first study of sintering of SFO by pSPS, the behaviour of SFO during consolidation was studied in detail. Namely, the necking of *SFO* particles during pSPS occurred already at lower temperatures (1100 °C) and shorter dwell times (5 min) compared to conventional sintering (1200 °C/4 h) [22]. With the increase of sintering temperature, the sample densities increased, but coercivity was substantially lowered. Based on the microstructural and phase analysis of samples coupled with diffusion couple experiment in air it was concluded that the reductive environment and/or the presence of carbon triggered the reduction of the main hard magnetic phase, resulting in the loss of hard magnetic properties. $SrFe_{12}O_{19}$ partially decomposes to Fe_3O_4 at 500 °C. At 600 °C a reduction of Fe_3O_4 to FeO, α-Fe, γ-Fe and $SrCO_3$ occurs. At 700 °C α-Fe, γ-Fe, $SrCO_3$, and FeO are present. FeO disappears at 800 °C, and the ratio between α-Fe and γ-Fe starts to favour the formation of γ-Fe. At 900 °C a metastable phase $Sr_4Fe_2(CO_3)O_6$ is formed. When reaching 1000 °C the HT-XRD detects the presence of only α-Fe, γ-Fe and $SrFeO_{x-3}$. Some of [those phases have lower melting points, inducing a shift in the sintering mechanism from solid-state sintering to a partial liquid-phase sintering mechanism.

CRediT authorship contribution statement

A. Učakar: Writing – review & editing, Writing – original draft, Visualization, Methodology, Investigation, Formal analysis, Conceptualization. **A. Kocjan:** Writing – review & editing. **B. Belec:** Investigation, Formal analysis, Data curation. **J. Košir:** Investigation, Formal analysis, Data curation. **T. Kallio:** Resources, Investigation, Funding acquisition, Formal analysis, Data curation. **M. Kržmanc Maček:** Investigation, Formal analysis, Data curation. **B. Arah:** Investigation, Formal analysis, Data curation. **P. Jenuš Belec:** Writing – review & editing, Writing – original draft, Validation, Supervision, Resources, Project administration, Methodology, Investigation, Funding acquisition, Formal analysis, Data curation, Conceptualization.

Declaration of competing interest

Authors of Manuscript Number: OCERAM 100804 entitled "The Role of Carbon Presence on the Strontium Hexaferrite Phase Decomposition During Pressureless Spark Plasma Sintering (pSPS)" by Aleksander Učakar et al., declare there is no conflict of interest.

Acknowledgements

The authors would like to thank the Slovenian Research Agency for funding the research programs P2-0405, P2-0087, PR-05722 and Business Finland for the NextGenBat project (No. 211849).

Supplementary materials

Supplementary material associated with this article can be found, in the online version, at doi:10.1016/j.oceram.2025.100804.

References

[1] S. Hirosawa, Current status of research and development toward permanent magnets free from critical elements, J. Magn. Soc. Jpn. 39 (3) (2015) 85–95, https://doi.org/10.3379/msjmag.1504r004.
[2] S.D. Bhame, P.A. Joy, Effect of sintering conditions and microstructure on the magnetostrictive properties of cobalt ferrite, J. Am. Ceram. Soc. 91 (6) (2008) 1976–1980, https://doi.org/10.1111/j.1551-2916.2008.02367.x.
[3] R. Vinaykumar, J. Bera, Low-temperature sintering of SrCo1.5Ti1.5Fe9O19 ferrite and its characterization for X-band antenna application, J. Alloys Compd. 790 (2019) 413–420, https://doi.org/10.1016/j.jallcom.2019.03.168.
[4] P. Jenuš, On the potential of hard ferrite ceramics for permanent magnet technology – A review on sintering strategies, J. Phys. D. Appl. Phys. (2020).
[5] A.-K. Hofer, A. Kocjan, R. Bermejo, High-strength lithography-based additive manufacturing of ceramic components with rapid sintering, Addit. Manuf. 59 (June) (2022) 103141, https://doi.org/10.1016/j.addma.2022.103141.
[6] D. Li, *Rapid sintering of ceramics by intense thermal radiation*, no. February. 2016.
[7] D. Li, Y. Liu, Y. Zhong, L. Liu, E. Adolfsson, Z. Shen, Dense and strong ZrO 2 ceramics fully densified in <15 min, Adv. Appl. Ceram. 118 (1–2) (2019) 23–29, https://doi.org/10.1080/17436753.2018.1449580.
[8] P. Sharma, A. Verma, R.K. Sidhu, O.P. Pandey, Process parameter selection for strontium ferrite sintered magnets using Taguchi L9 orthogonal design, J. Mater. Process. Technol. 168 (1) (2005) 147–151, https://doi.org/10.1016/j.jmatprotec.2004.12.003.
[9] F. Mazaleyrat, A. Pasko, A. Bartok, M. Lobue, Giant coercivity of dense nanostructured spark plasma sintered barium hexaferrite, J. Appl. Phys. 109 (7) (2011), https://doi.org/10.1063/1.3556918.
[10] P. Jenuš, et al., Magnetic performance of SrFe 12 O 19 – Zn 0 . 2 Fe 2 . 8 O 4 hybrid magnets prepared by spark plasma sintering, J. Phys. D. Appl. Phys. 54 (2021).
[11] N. Langhof, D. Seifert, M. Göbbels, J. Töpfer, Reinvestigation of the Fe-rich part of the pseudo-binary system SrO-Fe2O3, J. Solid. State Chem. 182 (9) (2009) 2409–2416, https://doi.org/10.1016/j.jssc.2009.05.039.
[12] A.Z. Eikeland, M. Stingaciu, A.H. Mamakhel, M. Saura-Múzquiz, M. Christensen, Enhancement of magnetic properties through morphology control of SrFe12O19 nanocrystallites, Sci. Rep. 8 (1) (2018) 1–9, https://doi.org/10.1038/s41598-018-25662-8.
[13] B.H. Toby, R.B. Von Dreele, GSAS-II: the genesis of a modern open-source all purpose crystallography software package, J. Appl. Crystallogr. 46 (2) (2013) 544–549, https://doi.org/10.1107/S0021889813003531.
[14] R.I. Todd, et al., Electrical characteristics of flash sintering: thermal runaway of joule heating, J. Eur. Ceram. Soc. 35 (2015) 1865–1877.
[15] Abaqu, "'Cavity radiation," section 32.1.1 of the ABAQUS Analysis User's Manual', *manual*.
[16] S. Ovtar, S.Le Gallet, L. Minier, N. Millot, D. Lisjak, Control of barium ferrite decomposition during spark plasma sintering: towards nanostructured samples with anisotropic magnetic properties, J. Eur. Ceram. Soc. 34 (2) (2014) 337–346, https://doi.org/10.1016/j.jeurceramsoc.2013.07.027.
[17] T. Jantzen, S. Petersen, K. Hack, Thermodynamic assessment of the Fe–Sr–O system with special attention to the Perovskite phase, Chem. Eng. Sci. 211 (2020) 115271, https://doi.org/10.1016/j.ces.2019.115271.
[18] H. Okamoto, Phase diagrams for binary alloys, ASM Int (2010) 1752.
[19] R.C. Pullar, Hexagonal ferrites: a review of the synthesis, properties and applications of hexaferrite ceramics, Prog. Mater. Sci. 57 (7) (2012) 1191–1334, https://doi.org/10.1016/j.pmatsci.2012.04.001.
[20] E. Bagherisereshki, J. Tran, F. Lei, N. AuYeung, Investigation into SrO/SrCO3 for high temperature thermochemical energy storage, Sol. Energy 160 (November 2017) (2018) 85–93, https://doi.org/10.1016/j.solener.2017.11.073.

[21] A. Fossdal, M.A. Einarsrud, T. Grande, Phase equilibria in the pseudo-binary system SrO-Fe2O 3′, J. Solid State Chem. 177 (8) (2004) 2933–2942, https://doi.org/10.1016/j.jssc.2004.05.007.
[22] F. Kools, *Science and technology of ferrite magnets; modelling of coercivity and grain growth inhibition*, vol. 2, no. 2003. 2003.
[23] E. Peng, X. Wei, T.S. Hemg, U. Garbe, D. Yu, J. Ding, Ferrite-based soft and hard magnetic structures by extrusion free-forming, RSC Adv. 7 (2017) 27128.
[24] F. Yang, X. Zhang, Z. Guo, A.A. Volinsky, 3D gel-printing of Sr ferrite parts, Ceram. Int. 44 (2018).
[25] M. Harmer, B. Rj, Fast firing – microstructural benefits. FAST FIRING – Microstruct, Benefits (1981).
[26] M. Harmer, R. Ew, B. Rj, Rapid sintering of pure and doped alpha – AL2O3, RAPID sinter, Pure Doped Alpha _AL2O3 (1979).
[27] A. Klein, D. Hotza, Advanced ceramics with dense and fine-grained microstructures through fast firing, Rev. Adv. Mater. Sci. 30 (Jun) (2012).
[28] J. Smit, H.P.J. Wijn, Physical properties of ferrites, in: Advances in Electronics and Electron Physics, 6, Academic Press, 1954, pp. 69–136.
[29] M. Jin, X. Wang, Z. Wang, et al., Effects of atmosphere on the microstructure and magnetic properties of strontium ferrites with microwave-assisted sintering, J. Supercond. Nov. Magn. 28 (2015) 3059–3063, https://doi.org/10.1007/s10948-015-3117-3.
[30] C. Bohlender, M. Kahnes, R. Müller, J. Töpfer, Phase formation, magnetic properties, and phase stability in reducing atmosphere of M-type strontium hexaferrite nanoparticles synthesized via a modified citrate process, J. Mater. Sci. 54 (2019) 1136–1146.
[31] Saeed, Z., & Azhdar, B. (2022). Influence of high temperature on the crystal structure of SrFe12O19 nanoparticle. 2022(1), 5467020.